

The correlation between the velocity of Si 6355 at maximum and the late-time Ni-to-Fe ratio for SNe Ia

JIALIAN LIU¹

¹*Physics Department, Tsinghua University, Beijing 100084, China*

ABSTRACT

The late-time spectra of Type Ia Supernovae (SNe Ia) are important in studying the physics of their explosions. Multi-Gaussian fits are used to determine the velocity shifts and relative line fluxes of prominent emission lines ([Fe II] and [Ni II]) in the $\sim 7000\text{--}7500$ Å region on 61 nebular phase spectra of 34 SNe Ia. The relative line flux ratios are used to estimate the Ni-to-Fe ratios and a positive correlation between the velocities of Si λ 6355 at maximum and late-time Ni-to-Fe ratios is found for SNe Ia with redshifted or blueshifted nebular velocities. The correlation implies that SNe Ia with normal Si II velocities at maximum and redshifted nebular velocities can be interpreted as the maximum Si II velocities of all viewing angle are normal, possibly due to low metallicity.

Keywords: supernovae — general-methods — statistical

1. INTRODUCTION

It is widely accepted that type Ia supernovae (SNe Ia; see, e.g. [Filippenko 1997](#) for a review of supernova classification) resulted from thermonuclear explosion of a carbon-oxygen (CO) white dwarf ([Nomoto et al. 1997a](#); [Hillebrandt & Niemeyer 2000](#); [Maoz et al. 2014](#)). Proposed explosion scenarios are generally split into two progenitor systems: the single-degenerate scenario ([Whelan & Iben 1973](#)) with accretion-induced explosion of a massive WD with a non-degenerate companion, and the double-degenerate ([Iben & Tutukov 1984](#); [Webbink 1984](#)) scenario with merger-induced explosion of two white dwarfs. Numerical explosion models for explosion scenarios were proposed, such as the M_{ch} W7 models of [Nomoto et al. \(1997b\)](#) and [Iwamoto et al. \(1999\)](#), the M_{ch} DDT models of [Seitenzahl et al. \(2013\)](#), and the $Sub-M_{ch}$ detonation models of [Sim et al. \(2010\)](#) and [Shen et al. \(2018\)](#). However, none of the models entirely succeed to be consistent with observations. We still do not understand the explosion mechanism well.

Some early observational parameters, which reflect the characteristics of the outer region of the explosion ejecta, can be used to study the explosion mechanism. The decline parameter $\Delta m_{15}(B)$, the decline in magnitudes in the B band during the first 15 days postmaximum, has

a correlation with peak luminosity that brighter objects have a lower $\Delta m_{15}(B)$ than the dimmer ones ([Phillips 1993](#); [Phillips et al. 1999](#)). The velocity of Si II λ 6355 absorption can be used to deduce the photospheric velocity, which gives a direct indication of the kinetic energy of the explosion. [Benetti et al. \(2005\)](#) assigned SN Ia to three groups, Low Velocity Gradient (LVG), High Velocity Gradient (HVG) and Faint (FAINT), based on the velocity of Si II λ 6355 absorption measured 10 days past maximum $v_{10}(\text{Si II})$ and its gradient which is the average daily rate of decrease of the velocity of Si II λ 6355 absorption. [Wang et al. \(2009\)](#) divided a sample of SN Ia into two groups, Normal Velocity (NV) and High Velocity (HV), based on the velocity of Si II λ 6355 absorption at maximum $v_{10}(\text{Si II})$.

At phase of about more than 200 d after maximum, the outer ejecta become transparent and the inner region of the ejecta are visible, which can be used to probe the inner ejecta distributions. The 7300 Å region is an important region to measure the velocity, width and flux of [Fe II] and [Ni II]. [Maguire et al. 2018](#) use multi-Gaussian fit to measure the ratio of Ni to Fe abundance, which is an important parameter to test different explosion models (Figure 10 in [Maguire et al. 2018](#). [Maeda et al. 2010a](#) used the velocity of [Fe II] and [Ni II] to estimate the nebula velocity. Then [Maeda et al. 2010b](#) proposed an asymmetric explosion model based on their observation that the SNe Ia with high(low) velocity gradient \dot{v} tend to have redshift(blueshift) nebula velocity. However,

lines in this region are seriously blended, which cause difficulty to the measurement. Direct measurement (Silverman et al. 2013), Gaussian fit (Graham et al. 2017) and Multi-Gaussian fit (Seitenzahl et al. 2013) are used to fit the region and the results show that most cases are consistent with the correlation between \dot{v} and nebula velocity found by Seitenzahl et al. (2013). (Silverman et al. 2013) also found that the relation also holds if Si II velocities at maximum are used instead of velocity gradients, where HV correspond to high velocity gradients. At this point, however, some exceptions arise (e.g. ASASSN-14jg, Graham et al. 2017).

This work mainly attempts to study the potential correlations between the ratio of Ni to Fe abundance at late time and the Si II $\lambda 6355$ velocity, which might give some implication for the exceptions who have normal Si II velocities and redshifted nebula velocities. In addition, the correlation between the ratio of Ni to Fe abundance and decline parameter is also explored. We outline our data sources in Section 2. In Section 3, we show the fitting methods and the method used to roughly estimate the Ni/Fe ratio. The fitting results are also showed in Section 3. Findings are discussed in Section 4 and the conclusions are presented in Section 5.

2. DATA SOURCE

The analysis is performed on a sample of 61 spectra (~ 200 -430 d) of 34 SNe Ia and the parameters are listed in Table 1. The majority of the publicly available data were retrieved using the Open Supernova Catalog (OSC, Guillochon et al. 2017) and Weizmann Interactive Supernova data REpository (WiSeREP, Yaron & Gal-Yam 2012). The other late-time spectra come from SNDB (SN 2011fe and SN 2013dy, (Stahl et al. 2020), along with spectra of SN 2017fgc (Zeng et al. 2021), SN 2019ein (Gao, in prep) and SN 2019np (Sai, in prep). The majority of Si II $\lambda 6355$ velocities within ± 5 d of maximum come from Wang et al. (2019), Graham et al. (2017) and Maguire et al. (2018), supplemented with values for individual objects: SN 1986G and SN 1990N (estimated from (Benetti et al. 2005) using the Si II velocities and the velocity gradients), SN2008Q (Silverman et al. 2013), SN2011by (Foley et al. 2014), SN2013dy (Pan et al. 2015), SN2017cbv and SN2018oh (Graham et al. in prep), SN2017fgc (Burgaz et al. 2021), SN2019ein (Kawabata et al. 2020) and SN2019np (Sai, in prep). The majority of decline parameters and extinction come from Tucker et al. (2020), supplemented with values for individual objects: SN2015F (Graham et al. 2017), SN2017cbv and SN2018oh (Graham et al. in prep), SN2017fgc (Burgaz et al. 2021), SN2019ein (Kawabata et al. 2020)(Kawabata et al. 2020) and SN2019np (Sai,

in prep). R_v are assumed to be 3.1 except the samples listed in Table 2. To check the reliability of the results given by this work, a comparison with the Ni-to-Fe ratios of Flörs et al. (2020) is performed in Section 4.

3. METHOD

3.1. Fitting methods

In the 7300 Å region, the nebula spectra of SNe Ia are dominated by [Fe II] (7155, 7172, 7388, 7453 Å) and [Ni II] (7378, 7412 Å), and possibly [Ca II] (7291, 7324 Å) (Maguire et al. 2018). I follow the fitting method used by Maguire et al. (2018), in which gaussian profiles are used to fit the emission lines and [Ca II] are excluded from the components. Although there are six gaussian components including [Fe II] (7155, 7172, 7388, 7453 Å) and [Ni II] (7378, 7412 Å), the number of parameters is the same with a double gaussian fitting, assuming that for the features of the same element and ionization state in the 7300 Å region, the width and velocities are equal and the relative strength is given by Jerkstrand et al. (2015) using the radiative transition rates and the assumption of LTE level populations as well as an optically-thin approximation. The pseudo-continuum is defined as a straight line connecting the red and blue points of the spectral region chosen interactively. Before measuring the features, the spectra were smoothed with a Savitsky-Golay filter of window size ~ 20 -50 Å using the scipy package's `signal.savgolfilter` function. Subtracting the continuum, the fitting function can be written as

$$\begin{aligned}
 I(\lambda) = & A_{Fe} \exp \left[-\frac{(\lambda - 7155t_{Fe})^2}{2\sigma_{Fe}^2} \right] \\
 & + 0.24A_{Fe} \exp \left[-\frac{(\lambda - 7172t_{Fe})^2}{2\sigma_{Fe}^2} \right] + 0.19A_{Fe} \exp \left[-\frac{(\lambda - 7388t_{Fe})^2}{2\sigma_{Fe}^2} \right] \\
 & + 0.31A_{Fe} \exp \left[-\frac{(\lambda - 7453t_{Fe})^2}{2\sigma_{Fe}^2} \right] + A_{Ni} \exp \left[-\frac{(\lambda - 7378t_{Ni})^2}{2\sigma_{Ni}^2} \right] \\
 & + 0.31A_{Ni} \exp \left[-\frac{(\lambda - 7412t_{Ni})^2}{2\sigma_{Ni}^2} \right]
 \end{aligned} \tag{1}$$

where λ is the wavelength, t_{Fe} and t_{Ni} represent the velocities, σ_{Fe} and σ_{Ni} represent the width, A_{Fe} and A_{Ni} represent the strength of the emission lines. Specifically, velocity v_i and full width half maximum w_i can be obtained by $v_i = (t_i - 1) \times 300000 \text{ km s}^{-1}$, $w_i = 2 \times \frac{300000}{\lambda_i} \times \sqrt{2 \ln 2} \text{ km s}^{-1}$, where $i = Fe$ for [Fe II] $\lambda 7155$ and $i = Ni$ for [Ni II] $\lambda 7378$, λ_i are the rest wavelength of the features. The only boundary of these parameters is that the FWHM of [Ni II] 7378 is limited to $\leq 13000 \text{ km s}^{-1}$, which is also adopted by Graham et al. (in prep). The integrated flux ratio of [Ni II] $\lambda 7378$ to [Fe II] $\lambda 7155$ are given by A_{Ni}/A_{Fe} , σ_{Ni} and σ_{Fe} as $R_{flux} = A_{Ni}\sigma_{Ni}/A_{Fe}\sigma_{Fe}$.

The uncertainties were calculated using a Monte-Carlo approach. The interactively chosen continuum values were varied by random amounts up to 10 Å to the blue

and red of this value and then the fitting was then repeated. If the flux ratio is too large or too small compared with the best fit one, the result will be rejected. This process is repeated until 1000 results are received for each spectrum and then the standard deviation was calculated to estimate the uncertainty. An additional uncertainty on the of 200 km s^{-1} was added on the velocity measurement due to the peculiar velocity effects of the host galaxies.

The fitting line velocities, FWHM, integrated flux ratio their errors are list in 3. The results show that the velocity of [Ni II] is obviously bluer than that of [Fe II] and the [Ni II] is too wide for some cases, which is also mentioned by Graham et al. (in prep) and interpreted as the fitting method gives bluer and wider [Ni II] lines when [Ni II] lines are allowed to contribute to the blue-half of the feature. Graham et al. (in prep) used a two-stage minimum-Ni method, which fits iron to the blue half of the feature first and then allow nickel to make up the rest of the flux in the blended feature, to estimate the minimum amount of nickel and found the method possibly more accurate since the iron and nickel have more similar velocities from this method. Different from the method of Graham et al. (in prep), I propose another two-stage improved multi-Gaussian fit which divides the fit to two steps: (1) Remove the middle region of the spectrum $\sim 7250\text{-}7350 \text{ \AA}$ and fit. (2) Fix the [Ni II] lines given by the first step and fit the original spectrum to get the parameters of [Fe II] emission lines. The purpose of the first step is to reduce the contribution from nickel to the middle region that the peak of the broad nickel usually locates in. The range of the middle part is set alternatively to get the [Ni II] lines redder and narrower and finally get a best fit. The results given by the improved method are listed in 4.

3.2. Rough nickel-to-iron ratio

The nickel-to-iron ratio is estimated following the method of Maguire et al. (2018),

$$\frac{n_{Ni II}}{n_{Fe II}} = \frac{L_{7378}}{L_{7155}} \exp\left(-\frac{0.28}{kT}\right) \frac{d_{C_{Fe II}}}{d_{C_{Ni II}}} / 4.9 \quad (2)$$

where $\frac{d_{C_{Fe II}}}{d_{C_{Ni II}}}$ is the departure coefficients, $\frac{L_{7378}}{L_{7155}}$ is the ratio of luminosity, k is Boltzmann constant and T is the temperature.

In this work I use the ratio of the integrated flux of [Ni II] $\lambda 7378$ and [Fe II] $\lambda 7155$ to estimate the nickel-to-iron abundance ratio. To obtain an estimated nickel-to-iron ratio, the departure coefficients $\frac{d_{C_{Fe II}}}{d_{C_{Ni II}}}$ is assumed to be 1.8, the mean ratio $\frac{n_{Ni II}}{n_{Fe II}}$ is calculated by integrating from $T = 3000\text{K}$ to $T = 8000\text{K}$ and is assumed to

equal the ratio $\frac{n_{Ni}}{n_{Fe}}$. The uncertainty of $\frac{n_{Ni}}{n_{Fe}}$, which is generally much larger than the uncertainty from the fit, were estimated by varying the departure coefficients in the range 1.2~2.4, the ionization balance in the range of 0.8~1.2 from the model of Fransson & Jerkstrand (2015), the temperature in the range 3000-8000K and finally roughly set to be 50%. Figure 5 shows the nickel-to-iron ratio for the spectra presented in this study, which has a range about 0.02~0.20 covering all the models presented in Figure 10 of Maguire et al. (2018).

4. RESULTS AND DISCUSSION

Lentz et al. (2000) found that the blueward shift of the Si II feature increased with higher metallicity. Timmes et al. (2003) found that the radioactive ^{56}Ni decreased with higher metallicity. The ratio of stable to radioactive isotopes of Fe-group elements produced, which has positive correlation with the Ni-to-Fe ratio at the late time, depends on the central density of the white dwarf at the time of explosion (Höflich et al. 2004) and is an important parameter for explosion models. And the decline parameter decreases with more radioactive element ^{56}Ni since ^{56}Ni can increase the opacity. Here we discuss the connections between the early-time parameters Si II velocity, decline parameter and the late-time parameter Ni-to-Fe ratio. Before the main topics, we compare the results of different fitting methods.

4.1. Comparison between different methods

In Figure 1, I compare the emission line parameters measured from multi- and improved multi-Gaussian fits. The velocity of the nickel feature gets redder and the FWHM of the nickel feature gets narrower for many cases, which means the improved multi-Gaussian fit works. As a result, the ratio of Ni to Fe generally decreases. This can also be seen in 2, where I show the fit results of improved multi- and multi-Gaussian fits for a common SNe Ia SN 2011fe. (Flörs et al. 2020) apply NLTE models to fit this region and give the mass ratio of nickel to iron. The comparison between the ratio given by NLTE and improved multi-Gaussian fit is also showed in Figure 1. The ratio given by NLTE method is smaller than that given by the improved multi-Gaussian method for most cases. This is corresponding to the fact that most Ni-to-Fe ratios measured by Maguire et al. (2018) with a multi-Gaussian fit consistent with DDT while the ratios measured by (Flörs et al. 2020) with a detailed method consistent with Sub-Chandrasekhar. (Flörs et al. 2020) performs a more detailed fit, but Maguire et al. (2018) argues that super-solar sub-Mch models are needed to explain the Ni-to-Fe ratio since the sub-Mch models (Sim et al. 2010; Shen et al. 2018) show

that neutron-rich ^{58}Ni depends on the progenitor star metallicity and is not produced in the explosion. The difference needs more discussion but this is not the main topic in this work.

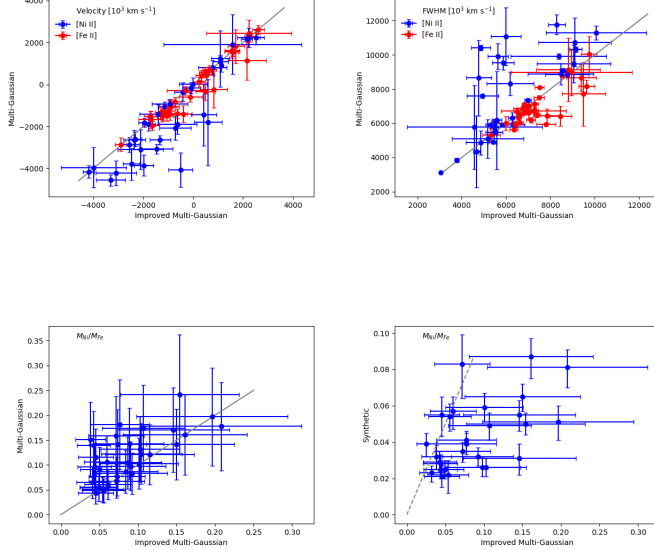


Figure 1. Panels show comparisons of the emission line parameters velocity (top left), FWHM (top right), and $M_{\text{Ni}}/M_{\text{Fe}}$ measured from multi- and improved multi-Gaussian fits to the [Fe II] 7155 Å and [Ni II] 7378 Å features for spectra presented in this work. The comparison of $M_{\text{Ni}}/M_{\text{Fe}}$ measured from the improved multi-Gaussian fits and the method of Flörs et al. (2020) is showed in bottom right panel.

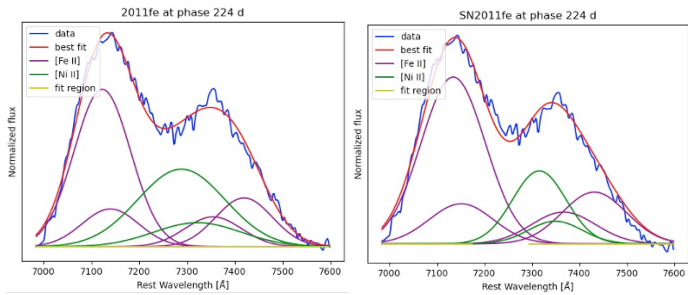


Figure 2. A comparison of multi-Gaussian (left) and improved multi-Gaussian (right) fits for the spectrum of SN 2011fe at 224d after the maximum. The blue line is the pseudo-continuum subtracted flux density at rest wavelengths; the purple and green lines show the best-fit iron and nickel features, respectively; and the red line shows the combined best fit.

4.2. Ni-to-Fe ratio evolution with phase

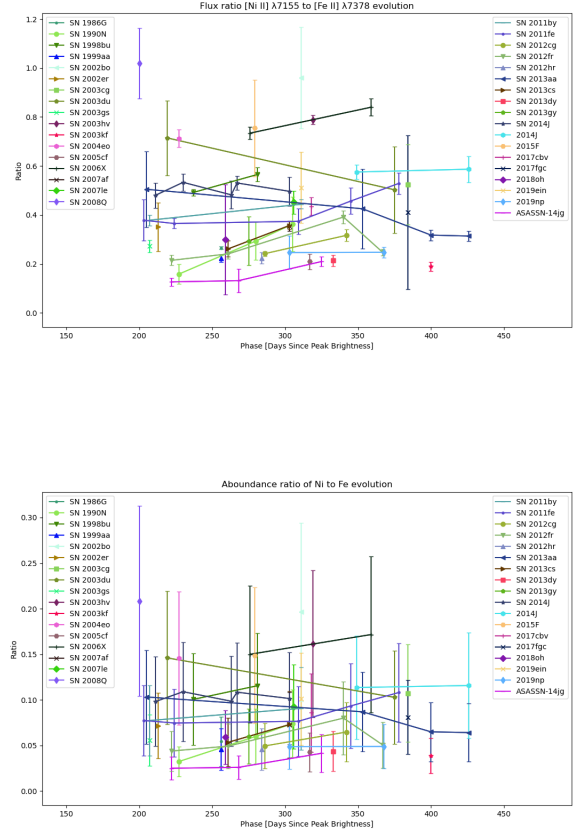


Figure 3. Evolution of integrated flux ratio of [Fe II] λ7155 to [Ni II] λ7378 (top) and abundance ratio of Ni to Fe (bottom, by mass) measured from an improved multi-Gaussian fit to the 7300 Å region over phase.

Figure 3 shows the evolution of integrated flux ratio of [Ni II] λ7378 to [Fe II] λ7155 measured from an improved multi-Gaussian fit and the corresponding abundance ratio of Ni to Fe for spectra presented in this work. The relative uncertainty of flux ratio is much smaller than 50% that is roughly set for the abundance ratio in 3.2 except several SNe Ia which have relatively low S/N spectra. Figure 10 of Maguire et al. (2018) shows that the Ni-to-Fe ratio has a slow evolution for all models and decreases over time since left ^{56}Ni continue to decay and finally produce ^{56}Fe . However, some samples in this work show an increasing Ni-to-Fe ratio with phase. This can be due to the light-echo, which is mentioned by Flörs et al. (2020) for the increasing Ni-to-Fe ratio of SN 1998bu. The increasing Ni-to-Fe ratio can also be due to the increasing [Ni II]/[Ni III] (but why this ratio

can increase?). Since the phase ranges from 200d to 400d for most samples and the ratio evolution in this work is slow, parameters given by the spectrum closest to 300d are chosen to do the following analyses for each SNe Ia.

4.3. Connection between the Ni-to-Fe ratio and the Si II velocity

Silverman et al. (2013) extended the results of Maeda et al. (2010a) and found that SNe Ia displays redshift late-time 7300 Å region spectral features have higher Si II velocity that are more than 11,800 km s⁻¹ (HV, Wang et al. 2009). We focus on [Fe II] λ7155 feature velocity as Maguire et al. (2018) do in the further analysis.

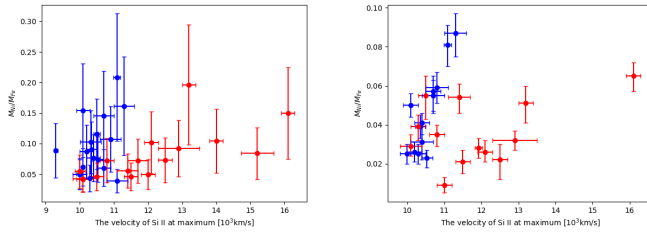


Figure 4. Mass ratios of Ni and Fe measured from an improved multi-Gaussian (left) and the method of Flörs et al. (2020) (right) vs. velocities of Si II λ6355 at maximum. Samples with redshift (blueshift) [Fe II] feature are showed in red (blue).

Figure 4 shows the correlation between the ratio of nickel to iron abundance at the phase closest to 300 day in this study and the velocity of Si II λ7378 at maximum $v_0(\text{Si II})$ in table 1. The samples with redshift [Fe II] λ7155 features are plotted in red and the samples with blueshift [Fe II] λ7155 features are plotted in blue. Ni-to-Fe ratios measured from the improved multi-Gaussian are shown in the left panel of Figure 4. All the HV samples in this work have redshift [Fe II] λ7155 features, while some NV samples also have redshift [Fe II] λ7155 features which is inconsistent with the expectation for NV SNe Ia of Silverman et al. (2013). However, the panel shows that red points and blue points are not mixed except the left-bottom region and the Ni-to-Fe ratio increases with higher Si II velocity for SNe Ia with blueshift [Fe II] λ7155 features and redshift [Fe II] λ7155 features respectively. This positive correlation is consistent with the combinational conclusion of Lentz et al. (2000) and Timmes et al. (2003) that higher metallicity leads to higher Si II velocity and more stable ⁵⁸Ni, namely higher Ni-to-Fe ratio and this would lead to positive correlation between Si II velocity and Ni-to-Fe ratio. The respective positive corre-

lation firmly supports the asymmetric explosion model of Maeda et al. (2010b) without which the correlation will be a simple positive correlation including the SNe Ia with redshift and blueshift [Fe II] features. The correlation between Ni-to-Fe ratio and Si II velocity can be used to explain the SNe Ia inconsistent with the asymmetric model which have redshift [Fe II] λ7155 features and low Si II velocity, as long as the Ni-to-Fe ratio, namely the metallicity, is low enough that the maximum Si II velocity of all viewing angle is small.

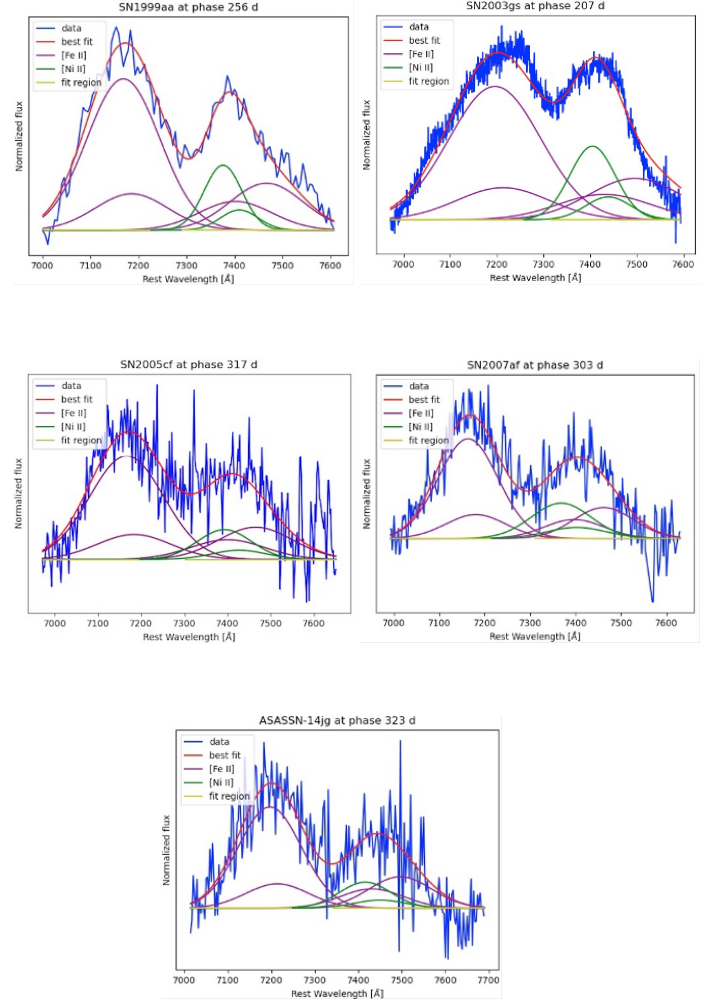


Figure 5. Best fits to the 7300 Å region containing [Fe II] and [Ni II] features for SN 1999aa, SN 2003gs, SN 2005cf, SN 2007af and ASASSN-14jg. The observed spectra are shown in blue, the overall fits are shown in red, the [Fe II] features are showed in purple and the [Ni II] features are showed in green. The fit region corresponds to the first step of improved multi-Gaussian fits.

However, the Ni-to-Fe ratio results of Flörs et al. (2020) shows a slightly different result that five SNe Ia which belongs to NV and show redshift [Fe II] $\lambda 7155$ features have higher Ni-to-Fe ratio compared with the HV. Figure 5 shows the fit for the five SNe Ia using the improved multi-Gaussian method. Only the spectrum of SN 2003gs fits not well, thus I consider SN 2003gs as a certain exception. Notice that the spectrum of SN 2003gs at 207d is peculiar compared with other 4 spectra that its features are ‘crooked’ and asymmetric and gaussian components cannot fit well. Besides, the height of the redward peak is close to that of the blueward peak for SN 2003gs while the height of the redward peak is smaller than that of the blueward peak for the other 4 spectra, which supports the high Ni-to-Fe ratio for SN 2003gs. And the width of the redward feature is wide for 91bg-like SN 2003gs, which is inconsistent with Silverman et al. (2013). Thus, SN 2003gs appears peculiar and cannot be explained by the correlation between Ni-to-Fe ratio and Si II velocity.

4.4. Connection between the Ni-to-Fe ratio and the decline parameter

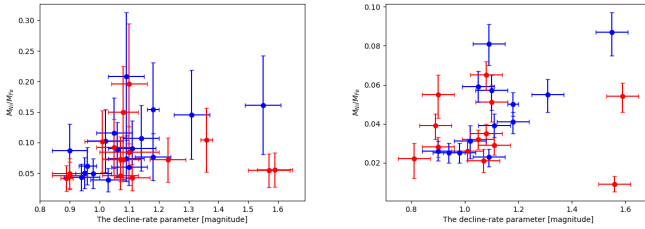


Figure 6. Mass ratios of Ni and Fe measured from an improved multi-Gaussian (left) and the method of Flörs et al. (2020) (right) vs. decline parameters. Samples with redshift (blueshift) [Fe II] feature are showed in red (blue).

Figure 6 shows the correlation between the ratio of nickel to iron abundance at the phase closest to 300 day in this study and the decline parameter $\Delta m_{15}(B)$ in table 1. Different from Figure 4, red points and blue

points are fully mixed in Figure 6 which implies that the viewing angle has little effect on the decline parameter. Figure 6 shows that the Ni-to-Fe ratio increases with larger decline parameter since higher decline parameter means less ^{56}Ni and less ^{56}Fe at late time. However, some points appear in the right-bottom region which have large decline parameter and small Ni-to-Fe ratio. In the left panel of Figure 6 (improved multi-Gaussian fit), SN 1986G and SN 2003gs are in the right-bottom region. In the right panel of Figure 6 (Flörs’s method), SN2012ht is in the right-bottom region and SN 2003gs is near this region. Notice that all the three SNe Ia are 91bg-like, it is likely that 91bg-like SNe Ia have low luminosity, large decline parameter and low Ni-to-Fe ratio at late time. This implies that 91bg-like SNe Ia locate in low metallicity environment and have low central density when they explode, which is consistent with the fact that 91bg-like SNe Ia are most found in old stellar population (Panther et al. 2019) where the metallicity is low.

5. CONCLUSION

In this paper, we have analyzed the connection between the Ni-to-Fe ratio at late time and the early-time parameters Si II velocity and decline parameter. Si II velocities and decline parameters come from literatures. We have proposed an improved multi-Gaussian fit and performed the fit to 7300Å region of 61 spectra of 34 SNe Ia to get the Ni-to-Fe ratios. As a comparison, the Ni-to-Fe ratios measured from the detailed method of Flörs et al. (2020) are used to do the same analysis. Our main results are: (i) Late-time Ni-to-Fe ratios can increase over time. (ii) Ni-to-Fe ratios at late time increases with higher Si II velocities for SNe Ia with redshift or blueshift [Fe II] $\lambda 7155$ features (Figure 4). This correlation supports the asymmetric explosion models of Maeda et al. (2010b) and can be used to explain the SNe Ia which has redshift [Fe II] $\lambda 7155$ feature and normal Si II velocity that the maximum velocity of all viewing angle is normal. (iii) 91bg-like SNe Ia tend to have low Ni-to-Fe ratios (Figure 6), which is consistent with the fact that they are most found in old stellar population (Panther et al. 2019) where the metallicity is low.

REFERENCES

- Amanullah, R., Goobar, A., Johansson, J., et al. 2014, ApJL, 788, L21, doi: [10.1088/2041-8205/788/2/L21](https://doi.org/10.1088/2041-8205/788/2/L21)
- Benetti, S., Cappellaro, E., Mazzali, P. A., et al. 2005, ApJ, 623, 1011, doi: [10.1086/428608](https://doi.org/10.1086/428608)
- Blondin, S., Matheson, T., Kirshner, R. P., et al. 2012, AJ, 143, 126, doi: [10.1088/0004-6256/143/5/126](https://doi.org/10.1088/0004-6256/143/5/126)
- Brown, P. J., Smitka, M. T., Wang, L., et al. 2015, ApJ, 805, 74, doi: [10.1088/0004-637X/805/1/74](https://doi.org/10.1088/0004-637X/805/1/74)
- Burgaz, U., Maeda, K., Kalomeni, B., et al. 2021, MNRAS, 502, 4112, doi: [10.1093/mnras/stab254](https://doi.org/10.1093/mnras/stab254)
- Burns, C. R., Stritzinger, M., Phillips, M. M., et al. 2014, ApJ, 789, 32, doi: [10.1088/0004-637X/789/1/32](https://doi.org/10.1088/0004-637X/789/1/32)

- Childress, M. J., Hillier, D. J., Seitzzahl, I., et al. 2015, MNRAS, 454, 3816, doi: [10.1093/mnras/stv2173](https://doi.org/10.1093/mnras/stv2173)
- Elias-Rosa, N., Benetti, S., Cappellaro, E., et al. 2006, MNRAS, 369, 1880, doi: [10.1111/j.1365-2966.2006.10430.x](https://doi.org/10.1111/j.1365-2966.2006.10430.x)
- Filippenko, A. V. 1997, ARA&A, 35, 309, doi: [10.1146/annurev.astro.35.1.309](https://doi.org/10.1146/annurev.astro.35.1.309)
- Flörs, A., Spyromilio, J., Taubenberger, S., et al. 2020, MNRAS, 491, 2902, doi: [10.1093/mnras/stz3013](https://doi.org/10.1093/mnras/stz3013)
- Foley, R. J., & Kirshner, R. P. 2013, ApJL, 769, L1, doi: [10.1088/2041-8205/769/1/L1](https://doi.org/10.1088/2041-8205/769/1/L1)
- Foley, R. J., Fox, O. D., McCully, C., et al. 2014, MNRAS, 443, 2887, doi: [10.1093/mnras/stu1378](https://doi.org/10.1093/mnras/stu1378)
- Fransson, C., & Jerkstrand, A. 2015, ApJL, 814, L2, doi: [10.1088/2041-8205/814/1/L2](https://doi.org/10.1088/2041-8205/814/1/L2)
- Galbany, L., Moreno-Raya, M. E., Ruiz-Lapuente, P., et al. 2016, MNRAS, 457, 525, doi: [10.1093/mnras/stw026](https://doi.org/10.1093/mnras/stw026)
- Gao, J., Jiang, B. W., Li, A., Li, J., & Wang, X. 2015, ApJL, 807, L26, doi: [10.1088/2041-8205/807/2/L26](https://doi.org/10.1088/2041-8205/807/2/L26)
- Gomez, G., Lopez, R., & Sanchez, F. 1996, AJ, 112, 2094, doi: [10.1086/118166](https://doi.org/10.1086/118166)
- Graham, M. L., Kumar, S., Hosseinzadeh, G., et al. 2017, MNRAS, 472, 3437, doi: [10.1093/mnras/stx2224](https://doi.org/10.1093/mnras/stx2224)
- Guillochon, J., Parrent, J., Kelley, L. Z., & Margutti, R. 2017, ApJ, 835, 64, doi: [10.3847/1538-4357/835/1/64](https://doi.org/10.3847/1538-4357/835/1/64)
- Hillebrandt, W., & Niemeyer, J. C. 2000, ARA&A, 38, 191, doi: [10.1146/annurev.astro.38.1.191](https://doi.org/10.1146/annurev.astro.38.1.191)
- Höflich, P., Gerardy, C. L., Nomoto, K., et al. 2004, ApJ, 617, 1258, doi: [10.1086/425571](https://doi.org/10.1086/425571)
- Iben, I., J., & Tutukov, A. V. 1984, ApJS, 54, 335, doi: [10.1086/190932](https://doi.org/10.1086/190932)
- Iwamoto, K., Brachwitz, F., Nomoto, K., et al. 1999, ApJS, 125, 439, doi: [10.1086/313278](https://doi.org/10.1086/313278)
- Jerkstrand, A., Ergon, M., Smartt, S. J., et al. 2015, A&A, 573, A12, doi: [10.1051/0004-6361/201423983](https://doi.org/10.1051/0004-6361/201423983)
- Kawabata, M., Maeda, K., Yamanaka, M., et al. 2020, ApJ, 893, 143, doi: [10.3847/1538-4357/ab8236](https://doi.org/10.3847/1538-4357/ab8236)
- Lentz, E. J., Baron, E., Branch, D., Hauschildt, P. H., & Nugent, P. E. 2000, ApJ, 530, 966, doi: [10.1086/308400](https://doi.org/10.1086/308400)
- Maeda, K., Taubenberger, S., Sollerman, J., et al. 2010a, ApJ, 708, 1703, doi: [10.1088/0004-637X/708/2/1703](https://doi.org/10.1088/0004-637X/708/2/1703)
- Maeda, K., Benetti, S., Stritzinger, M., et al. 2010b, Nature, 466, 82, doi: [10.1038/nature09122](https://doi.org/10.1038/nature09122)
- Maguire, K., Taubenberger, S., Sullivan, M., & Mazzali, P. A. 2016, MNRAS, 457, 3254, doi: [10.1093/mnras/stv2991](https://doi.org/10.1093/mnras/stv2991)
- Maguire, K., Sim, S. A., Shingles, L., et al. 2018, MNRAS, 477, 3567, doi: [10.1093/mnras/sty820](https://doi.org/10.1093/mnras/sty820)
- Maoz, D., Mannucci, F., & Nelemans, G. 2014, ARA&A, 52, 107, doi: [10.1146/annurev-astro-082812-141031](https://doi.org/10.1146/annurev-astro-082812-141031)
- Nomoto, K., Iwamoto, K., & Kishimoto, N. 1997a, Science, 276, 1378, doi: [10.1126/science.276.5317.1378](https://doi.org/10.1126/science.276.5317.1378)
- Nomoto, K., Iwamoto, K., Nakasato, N., et al. 1997b, NuPhA, 621, 467, doi: [10.1016/S0375-9474\(97\)00291-1](https://doi.org/10.1016/S0375-9474(97)00291-1)
- Pan, Y. C., Foley, R. J., Kromer, M., et al. 2015, MNRAS, 452, 4307, doi: [10.1093/mnras/stv1605](https://doi.org/10.1093/mnras/stv1605)
- Panther, F. H., Seitzzahl, I. R., Ruiter, A. J., et al. 2019, PASA, 36, e031, doi: [10.1017/pasa.2019.24](https://doi.org/10.1017/pasa.2019.24)
- Pastorello, A., Taubenberger, S., Elias-Rosa, N., et al. 2007, MNRAS, 376, 1301, doi: [10.1111/j.1365-2966.2007.11527.x](https://doi.org/10.1111/j.1365-2966.2007.11527.x)
- Phillips, M. M., Simon, J. D., Morrell, N., et al. 2013, ApJ, 779, 38, doi: [10.1088/0004-637X/779/1/38](https://doi.org/10.1088/0004-637X/779/1/38)
- Seitzzahl, I. R., Ciaraldi-Schoolmann, F., Röpke, F. K., et al. 2013, MNRAS, 429, 1156, doi: [10.1093/mnras/sts402](https://doi.org/10.1093/mnras/sts402)
- Shappee, B. J., Piro, A. L., Stanek, K. Z., et al. 2018, ApJ, 855, 6, doi: [10.3847/1538-4357/aaa1e9](https://doi.org/10.3847/1538-4357/aaa1e9)
- Shen, K. J., Kasen, D., Miles, B. J., & Townsley, D. M. 2018, ApJ, 854, 52, doi: [10.3847/1538-4357/aaa8de](https://doi.org/10.3847/1538-4357/aaa8de)
- Silverman, J. M., Ganeshalingam, M., & Filippenko, A. V. 2013, MNRAS, 430, 1030, doi: [10.1093/mnras/sts674](https://doi.org/10.1093/mnras/sts674)
- Sim, S. A., Röpke, F. K., Hillebrandt, W., et al. 2010, ApJL, 714, L52, doi: [10.1088/2041-8205/714/1/L52](https://doi.org/10.1088/2041-8205/714/1/L52)
- Srivastav, S., Ninan, J. P., Kumar, B., et al. 2016, MNRAS, 457, 1000, doi: [10.1093/mnras/stw039](https://doi.org/10.1093/mnras/stw039)
- Stahl, B. E., Zheng, W., de Jaeger, T., et al. 2020, MNRAS, 492, 4325, doi: [10.1093/mnras/staa102](https://doi.org/10.1093/mnras/staa102)
- Timmes, F. X., Brown, E. F., & Truran, J. W. 2003, ApJL, 590, L83, doi: [10.1086/376721](https://doi.org/10.1086/376721)
- Tucker, M. A., Shappee, B. J., & Wisniewski, J. P. 2019, ApJL, 872, L22, doi: [10.3847/2041-8213/ab0286](https://doi.org/10.3847/2041-8213/ab0286)
- Tucker, M. A., Shappee, B. J., Vallely, P. J., et al. 2020, MNRAS, 493, 1044, doi: [10.1093/mnras/stz3390](https://doi.org/10.1093/mnras/stz3390)
- Wang, X., Chen, J., Wang, L., et al. 2019, ApJ, 882, 120, doi: [10.3847/1538-4357/ab26b5](https://doi.org/10.3847/1538-4357/ab26b5)
- Wang, X., Li, W., Filippenko, A. V., et al. 2008, ApJ, 675, 626, doi: [10.1086/526413](https://doi.org/10.1086/526413)
- Wang, X., Filippenko, A. V., Ganeshalingam, M., et al. 2009, ApJL, 699, L139, doi: [10.1088/0004-637X/699/2/L139](https://doi.org/10.1088/0004-637X/699/2/L139)
- Webbink, R. F. 1984, ApJ, 277, 355, doi: [10.1086/161701](https://doi.org/10.1086/161701)
- Whelan, J., & Iben, I. 1973, ApJ, 186, 1007, doi: [10.1086/152565](https://doi.org/10.1086/152565)
- Yaron, O., & Gal-Yam, A. 2012, PASP, 124, 668, doi: [10.1086/666656](https://doi.org/10.1086/666656)
- Zeng, X., Wang, X., Esamdin, A., et al. 2021, ApJ, 919, 49, doi: [10.3847/1538-4357/ac0e9c](https://doi.org/10.3847/1538-4357/ac0e9c)
- Zhang, K., Wang, X., Zhang, J., et al. 2018, MNRAS, 481, 878, doi: [10.1093/mnras/sty2289](https://doi.org/10.1093/mnras/sty2289)

Table 1. SNe Ia light curve and spectral parameters, host galaxy information, number of late-time spectra and the corresponding phases.

Name	Host galaxy	Redshift	E(B-V)	$\Delta m_{15}(B)$	$v_0(\text{Si II})$	N_{spec}	Phase	Ref.	Ref.
			(mag)	(mag)	1000 km s ⁻¹		d	$v_0(\text{Si II})$	LC
SN1986G	NGC 5128	0.001825	0.91±0.06	1.57±0.07	10.00±0.15	1	256	1	12
SN1990N	NGC 4639	0.003369	0.02±0.06	1.09±0.06	10.53±0.15	3	227-305	1	12
SN1998bu	NGC 3368	0.002992	0.41±0.06	1.05±0.06	10.50±0.10	2	237, 281	2	12
SN1999aa	NGC 2595	0.014907	-0.01±0.06	0.90±0.06	10.50±0.20	1	256,	2	12
SN2002bo	NGC 3190	0.0043	0.36±0.06	1.10±0.06	13.20±0.20	2	221, 375	2	12
SN2002er	UGC 10743	0.009063	0.16±0.06	1.23±0.06	11.70±0.20	1	311	2	12
SN2003cg	NGC 3169	0.004113	1.32±0.06	1.14±0.06	10.90±0.30	1	384	2	12
SN2003du	UGC 9391	0.006408	0.00±0.06	1.02±0.06	10.40±0.30	2	221, 375	2	12
SN2003gs	NGC 936	0.00477	0.00±0.06	1.59±0.06	11.40±0.30	1	207	2	12
SN2003hv	NGC 1201	0.005624	0.00±0.06	1.55±0.06	11.30±0.30	1	319	2	12
SN2003kf	PGC 18373	0.00739	-0.03±0.06	1.03±0.06	11.10±0.30	1	400	2	12
SN2004eo	NGC 6928	0.015718	0.01±0.06	1.31±0.06	10.70±0.30	1	227	2	12
SN2006X	NGC 4321	0.005294	1.38±0.06	1.08±0.05	16.10±0.20	2	276, 359	2	12
SN2007af	NGC 5584	0.005464	0.12±0.06	1.08±0.06	10.80±0.20	1	303	2	12
SN2007le	NGC 7721	0.006721	1.05±0.06	1.05±0.06	12.90±0.60	1	306	2	12
SN2008Q	NGC 524	0.0081	0.06±0.06	1.09±0.06	11.09±0.10	1	200	3	12
SN2011by	NGC 3972	0.002843	0.09±0.06	1.11±0.09	10.35±0.14	2	207, 311	4	12
SN2011fe	NGC 5457	0.000804	0.04±0.06	1.18±0.06	10.40±0.20	5	203-378	2	12
SN2012cg	NGC 4424	0.001458	0.20±0.06	0.98±0.06	10.00±0.20	2	286, 342	5	12
SN2012fr	NGC 1365	0.004	-0.02±0.06	0.90±0.06	12.00±0.20	4	222-367	5	12
SN2012hr	PGC 18880	0.008	0.00±0.06	1.07±0.06	11.50±0.20	1	284	6	12
SN2013aa	NGC 5643	0.003999	0.02±0.06	0.90±0.06	10.20±0.20	4	205-426	5	12
SN2013cs	ESO576-17	0.00924	0.08±0.06	0.81±0.06	12.50±0.20	2	261, 303	5	12
SN2013dy	NGC 7250	0.00389	0.10±0.06	0.94±0.06	10.30±0.20	1	333,	7	12
SN2013gy	NGC 1418	0.014023	0.20±0.06	1.10±0.06	10.70±0.20	1	275	6	12
SN2014J	NGC 3034	0.000677	1.22±0.06	1.01±0.06	12.10±0.20	7	211-426	2	12
SN2015F	NGC 2422	0.0049	0.02±0.06	1.18±0.02	10.10±0.20	1	295	6	6
SN2017cbv	NGC 5643	0.003999	0.01±0.03	1.18±0.06	9.30±0.06	5	203-378	8	8
SN2017fgc	NGC 0474	0.001458	0.32±0.02	0.98±0.06	15.20±0.20	2	286, 342	9	9
SN2018oh	UGC 04780	0.012	-0.06±0.04	1.07±0.06	10.10±0.10	1	284	8	8
SN2019ein	NGC 5353	0.007755	0.09±0.02	0.90±0.06	14.00±0.20	4	205-426	10	10
SN2019np	NGC 3254	?	?	?	10.00±0.10	2	261, 303	11	11
ASASSN-14jg	PGC128348	0.014827	0.03±0.06	0.89±0.06	10.30±0.20	1	295	5	12

NOTE—Reference: (1) [Benetti et al. \(2005\)](#); (2) [Wang et al. \(2019\)](#); (3) [Silverman et al. \(2013\)](#); (4) [Foley & Kirshner \(2013\)](#); (5) [Maguire et al. \(2018\)](#); (6) [Graham et al. \(2017\)](#); (7) [Pan et al. \(2015\)](#); (8) [Graham et al. in prep](#); (9) [Burgaz et al. \(2021\)](#); (10) [Kawabata et al. \(2020\)](#) (11) [Sai, in prep.](#) (12) [Tucker et al. \(2020\)](#).

Table 2. R_v values and references of SNe Ia whose R_v values are not assumed to be 3.1.

Name	R_v	Ref.
SN2002bo	1.2	Phillips et al. (2013)
SN2004eo	0.8	Burns et al. (2014)
SN2006X	1.5	Wang et al. (2008) ; Phillips et al. (2013) ; Burns et al. (2014)
SN2007le	1.6	Phillips et al. (2013) ; Burns et al. (2014)
SN2014J	1.5	Amanullah et al. (2014) ; Foley et al. (2014) ; Gao et al. (2015) ; Brown et al. (2015)
SN2017fgc	1.5	Burgaz et al. (2021)
SN2019ein	1.5	Kawabata et al. (2020)

Table 3. Multi-Gaussian fit parameters of nebular-phase emission lines..

Name	Phase	[Fe II] Velocity	[Ni II] Velocity	[Fe II] FWHM	[Ni II] FWHM	Integrated Flux	Ref.
	[days]	[km s ⁻¹]	[km s ⁻¹]	[km s ⁻¹]	[km s ⁻¹]	Ni/Fe	Spec.
SN1986G	256	567±249	-1056±230	8795±81	3133±14	0.248±0.004	1
SN1990N	227	-1577±414	-4584±902	7243±431	5485±286	0.209±0.039	2
SN1990N	280	-1465±215	-3668±270	7500±94	10272±493	0.522±0.058	2
SN1990N	305	-1488±274	-4212±587	6761±174	10735±1425	0.689±0.127	2
SN1998bu	237	-1296±222	-1969±233	6872±149	4821±91	0.501±0.026	BSNIP
SN1998bu	281	-1345±277	-1885±321	7138±230	5754±64	0.589±0.025	BSNIP
SN1999aa	256	466±254	-160±251	7497±125	3829±120	0.214±0.011	BSNIP
SN2002bo	311	1563±302	1092±307	5318±397	5470±381	0.964±0.201	3
SN2002er	213	-232±885	-1447±1481	7710±1864	8649±2200	0.778±0.353	4
SN2003cg	384	-1408±283	-1422±470	8667±777	11290±415	0.852±0.322	5
SN2003du	219	-2011±244	-3377±367	6643±356	12143±1055	1.064±0.239	6
SN2003du	375	-1060±341	-3102±938	6634±376	9475±1097	0.645±0.122	6
SN2003gs	207	1813±803	1225±1335	10032±1030	4332±2102	0.238±0.224	BSNIP
SN2003hv	319	-2853±307	-4154±298	6993±223	5492±113	0.788±0.035	7
SN2003kf	400	-1402±387	-4061±823	8141±395	10419±153	0.740±0.112	CfA
SN2004eo	227	-839±242	-2862±349	6593±104	9105±38	0.834±0.017	8
SN2005cf	317	-348±400	-1803±2057	6417±580	11064±1680	0.680±0.208	BSNIP
SN2006X	276	2606±218	2160±225	7086±43	5905±33	0.692±0.008	BSNIP
SN2006X	359	2868±246	2335±242	8195±100	5620±106	0.735±0.022	BSNIP
SN2007af	303	415±258	-359±452	6696±215	6322±297	0.329±0.022	CfA
SN2007le	306	1618±252	794±335	6844±144	5912±131	0.406±0.022	BSNIP
SN2008Q	200	-1524±231	-1821±209	8091±61	4902±8	0.869±0.021	BSNIP
SN2011by	207	-1512±290	-3711±476	5698±172	7239±411	0.570±0.059	9
SN2011by	311	-1297±267	-2599±349	6340±155	6064±189	0.478±0.021	9
SN2011fe	203	-1069±454	-3081±800	6399±409	6896±1337	0.506±0.200	10
SN2011fe	224	-1359±409	-3655±716	5853±353	8763±1123	0.761±0.167	10
SN2011fe	309	-1396±228	-2647±224	5932±82	9527±393	0.885±0.071	10
SN2011fe	345	-1478±218	-3150±216	6194±57	10069±202	1.107±0.048	10
SN2011fe	378	-1604±237	-3397±230	6422±149	10751±729	1.276±0.236	10
SN2012cg	286	-1053±332	-2633±464	6687±194	6176±2860	0.272±0.233	11
SN2012cg	342	-1405±211	-3464±242	6357±86	10230±447	0.681±0.059	12
SN2012fr	222	2366±254	2528±566	6800±343	6179±443	0.250±0.025	13
SN2012fr	261	2269±237	2243±347	6458±165	5902±91	0.267±0.018	13
SN2012fr	340	2206±282	2238±295	7426±217	4995±147	0.360±0.023	13
SN2012fr	367	2113±248	3040±232	7830±119	4329±72	0.231±0.011	13
SN2012hr	284	108±244	-2077±565	6483±144	11765±574	0.565±0.037	13
SN2013aa	205	-1383±267	-4530±606	5986±145	10242±614	0.607±0.042	13
SN2013aa	353	-1422±276	-3793±743	5941±187	8865±628	0.512±0.073	12
SN2013aa	400	-1307±268	-3552±596	6378±181	9677±224	0.615±0.027	14
SN2013aa	426	-1161±406	-2770±782	7138±429	7028±2912	0.363±0.403	14
SN2013cs	261	1867±406	1702±1143	7016±522	6115±1017	0.307±0.046	14
SN2013cs	303	1555±216	897±289	6902±70	7335±94	0.377±0.013	12
SN2013dy	333	-1498±244	-3850±497	6197±155	9910±738	0.471±0.059	15
SN2013gy	275	-591±237	-1898±467	6428±400	8298±689	0.517±0.114	13
SN2014J	211	263±282	624±390	7098±400	8818±220	0.573±0.082	16
SN2014J	230	576±211	194±318	6960±70	10207±260	0.626±0.033	13
SN2014J	263	586±207	-243±247	6825±56	9456±104	0.518±0.016	10
SN2014J	267	474±220	53±389	6979±146	9998±656	0.604±0.102	17
SN2014J	303	692±214	12±302	7033±91	8859±182	0.504±0.023	10
SN2014J	349	804±252	1127±440	7605±307	9767±376	0.750±0.091	17
SN2014J	426	899±212	-77±221	8559±28	9579±15	0.645±0.005	18
SN2015F	279	-297±210	-938±230	6718±32	9913±154	1.179±0.035	14
SN2017cbv	318	-1256±211	-3069±236	6043±78	10318±158	0.699±0.023	19
SN2017fgc	384	2428±645	1909±1418	8961±1333	5763±2461	0.423±0.360	20
SN2018oh	259	-1678±425	-3952±963	6000±419	5094±1115	0.295±0.096	19
SN2019ein	310	1125±902	2223±458	9137±1846	4859±710	0.599±0.242	21
SN2019np	303	-1952±215	-4558±267	5607±36	7600±123	0.443±0.012	22
SN2019np	367	-1962±254	-4064±370	6079±178	7700±1053	0.530±0.156	22
ASASSN-14jg	221	1802±409	400±1483	6572±367	5133±1818	0.170±0.080	19
ASASSN-14jg	267	1817±239	1171±572	6738±138	7257±1263	0.221±0.058	14
ASASSN-14jg	323	1808±257	2602±419	8104±285	7902±902	0.327±0.066	23

NOTE—Reference: (1) Cristiani et al. (1992); (2) Gomez et al. (1996); (3) Blondin et al. (2012); (4) Kotak et al. (2005); (5) Elias-Rosa et al. (2006); (6) Stanishev et al. (2007); (7) Leloudas et al. (2009); (8) Pastorello et al. (2007); (9) Silverman et al. (2013); (10) Stahl et al. (2020) (11) Shappee et al. (2018) (12) Maguire et al. (2016); (13) Childress et al. (2015); (14) Graham et al. (2017); (15) Pan et al. (2015); (16) Galbany et al. (2016); (17) Srivastav et al. (2016); (18) Zhang et al. (2018); (19) Tucker et al. (2019); (20) Zeng et al. (2021); (21) Gao et al., in prep; (22) Sai et al., in prep; (23) Maguire et al. (2018).

Table 4. Improved multi-Gaussian fit parameters of nebular-phase emission lines..

Name	Phase	[Fe II] Velocity	[Ni II] Velocity	[Fe II] FWHM	[Ni II] FWHM	Integrated Flux	Ref.
	[days]	[km s ⁻¹]	[km s ⁻¹]	[km s ⁻¹]	[km s ⁻¹]	Ni/Fe	Spec.
SN1986G	256	483±255	-1129±234	8545±98	3045±33	0.265±0.005	1
SN1990N	227	-1292±407	-2998±1021	7900±401	6119±193	0.158±0.041	2
SN1990N	280	-1035±384	-2574±633	7842±327	7222±943	0.294±0.077	2
SN1990N	305	-1239±253	-3089±811	7285±167	9088±1637	0.362±0.111	2
SN1998bu	237	-1259±233	-1902±231	6964±82	4621±107	0.492±0.014	BSNIP
SN1998bu	281	-1278±251	-1774±250	7301±155	5466±191	0.565±0.029	BSNIP
SN1999aa	256	555±307	-81±350	7489±246	3762±99	0.223±0.014	BSNIP
SN2002bo	311	1565±306	1093±311	5325±398	5457±377	0.960±0.206	3
SN2002er	213	836±541	434±511	9494±976	4765±564	0.351±0.099	4
SN2003cg	384	-931±552	-1385±759	9394±674	10057±2272	0.525±0.164	5
SN2003du	219	-1660±383	-2297±339	6998±291	10557±2091	0.715±0.153	6
SN2003du	375	-887±336	-2105±904	7022±346	9055±1664	0.503±0.177	6
SN2003gs	207	1718±334	1090±362	9737±339	4661±150	0.272±0.025	BSNIP
SN2003hv	319	-2902±230	-4185±228	6991±70	5524±71	0.789±0.018	7
SN2003kf	400	-389±336	-501±479	9620±361	4853±429	0.189±0.019	CfA
SN2004eo	227	-721±260	-2550±382	6777±124	8557±133	0.713±0.036	8
SN2005cf	317	486±391	597±552	8458±490	5985±677	0.209±0.031	BSNIP
SN2006X	276	2612±228	2156±226	6807±99	5817±81	0.734±0.024	BSNIP
SN2006X	359	2734±256	2232±249	7800±123	5987±160	0.840±0.035	BSNIP
SN2007af	303	348±243	-402±337	6487±145	6289±216	0.354±0.021	CfA
SN2007le	306	1569±295	781±567	6730±399	6318±524	0.452±0.047	BSNIP
SN2008Q	200	-1706±261	-1950±228	7497±205	5398±179	1.020±0.144	BSNIP
SN2011by	207	-1175±243	-2874±308	6312±122	5238±224	0.378±0.022	9
SN2011by	311	-1165±233	-2323±267	6557±97	5513±169	0.444±0.018	9
SN2011fe	203	-1175±337	-2874±508	6312±261	5238±701	0.378±0.084	10
SN2011fe	224	-874±264	-2539±339	6675±150	5401±209	0.365±0.021	10
SN2011fe	309	-618±372	-1322±419	7803±433	5857±492	0.374±0.053	10
SN2011fe	345	-598±342	-1808±372	7791±347	6585±497	0.457±0.053	10
SN2011fe	378	-719±296	-2042±316	7868±247	7486±229	0.529±0.044	10
SN2012cg	286	-968±258	-2347±440	6900±160	5578±225	0.242±0.009	11
SN2012cg	342	-799±267	-1829±333	7476±144	6591±320	0.317±0.024	12
SN2012fr	222	2413±261	2955±328	7054±257	5171±245	0.214±0.021	13
SN2012fr	261	2294±239	2530±322	6618±164	5300±220	0.241±0.020	13
SN2012fr	340	2178±267	2185±272	7308±171	5295±211	0.391±0.027	13
SN2012fr	367	2106±255	2984±243	7764±164	4577±72	0.246±0.013	13
SN2012hr	284	231±255	-716±629	7380±151	8277±387	0.223±0.023	13
SN2013aa	205	-1379±232	-4367±387	6024±86	9862±1732	0.505±0.155	13
SN2013aa	353	-1232±255	-2469±334	6397±117	8459±1483	0.425±0.163	12
SN2013aa	400	-828±248	-2124±307	7190±124	6593±278	0.318±0.022	14
SN2013aa	426	-844±257	-1912±321	8014±114	7808±368	0.314±0.021	14
SN2013cs	261	1889±273	2310±791	7321±276	5109±480	0.262±0.033	14
SN2013cs	303	1599±212	1126±63	6921±89	6968±148	0.357±0.016	12
SN2013dy	333	-1050±258	-1967±385	7120±204	5619±460	0.214±0.023	15
SN2013gy	275	-98±450	-615±757	7845±580	6175±1064	0.293±0.100	13
SN2014J	211	268±269	321±391	7209±294	8482±98	0.480±0.051	16
SN2014J	230	593±225	-11±345	6973±80	9425±317	0.533±0.035	13
SN2014J	263	616±259	-170±451	6854±201	9004±968	0.482±0.056	10
SN2014J	267	510±225	-126±269	6899±140	9079±135	0.530±0.028	17
SN2014J	303	664±276	2±550	7010±238	8758±975	0.496±0.059	10
SN2014J	349	701±248	446±316	7226±172	8311±128	0.575±0.030	17
SN2014J	426	1033±358	573±334	8655±368	8756±779	0.587±0.054	18
SN2015F	279	-292±750	-928±718	7241±1477	8362±2145	0.754±0.197	14
SN2017cbv	318	-980±246	-1462±649	6605±145	9134±269	0.435±0.037	19
SN2017fgc	384	2246±1702	1593±2762	8952±2720	4568±3049	0.410±0.315	20
SN2018oh	259	-1689±505	-3987±1313	5983±591	5176±1613	0.299±0.224	19
SN2019ein	310	2167±772	2223±448	8797±1443	4859±681	0.512±0.145	21
SN2019np	303	-1633±288	-3305±575	6344±180	4932±713	0.246±0.067	22
SN2019np	367	-1484±269	-2914±350	7055±241	4502±230	0.247±0.022	22
ASASSN-14jg	222	1747±252	928±468	7095±128	4095±567	0.126±0.017	19
ASASSN-14jg	268	1812±337	601±1083	6660±289	4635±1584	0.132±0.047	14
ASASSN-14jg	325	1741±258	1527±275	7145±198	5667±243	0.210±0.019	23

NOTE—Reference: (1) Cristiani et al. (1992); (2) Gomez et al. (1996); (3) Blondin et al. (2012); (4) Kotak et al. (2005); (5) Elias-Rosa et al. (2006); (6) Stanishev et al. (2007); (7) Leloudas et al. (2009); (8) Pastorello et al. (2007); (9) Silverman et al. (2013); (10) Stahl et al. (2020) (11) Shappee et al. (2018) (12) Maguire et al. (2016); (13) Childress et al. (2015); (14) Graham et al. (2017); (15) Pan et al. (2015); (16) Galbany et al. (2016); (17) Srivastav et al. (2016); (18) Zhang et al. (2018); (19) Tucker et al. (2019); (20) Zeng et al. (2021); (21) Gao et al., in prep; (22) Sai et al., in prep; (23) Maguire et al. (2018).